Published in final edited form as:

Mol Cancer Res. 2022 August 05; 20(8): 1193–1207. doi:10.1158/1541-7786.MCR-21-1039.

Loss of PBRM1 alters promoter histone modifications and activates ALDH1A1 to drive renal cell carcinoma

David A. Schoenfeld[1,*], **Royce Zhou**[2,*], **Sakellarios Zairis**[3], **William Su**[2], **Nicole Steinbach**[2], **Deepti Mathur**[2], **Ankita Bansal**[2], **Alexis L. Zachem**[2], **Bertilia Tavarez**[2], **Dan Hasson**[2], **Emily Bernstein**[2], **Raul Rabadan**[3], **Ramon Parsons**[2]

[1]Section of Medical Oncology, Yale School of Medicine, New Haven, CT, USA

[2]Department of Oncological Sciences, The Tisch Cancer Institute, Icahn School of Medicine at Mount Sinai, New York, NY, 10029, USA

[3]Department of Systems Biology, Columbia University, New York, NY, 10032, USA

Abstract

Subunits of SWI/SNF chromatin remodeling complexes are frequently mutated in human malignancies. The PBAF complex is composed of multiple subunits, including the tumor suppressor protein PBRM1 (BAF180), as well as ARID2 (BAF200), that are unique to this SWI/SNF complex. *PBRM1* is mutated in various cancers, with a high mutation frequency in clear cell renal cell carcinoma (ccRCC). Here, we integrate RNA-seq, histone modification ChIP-seq, and ATAC-seq data to show that loss of PBRM1 results in *de novo* gains in H3K4me3 peaks throughout the epigenome including activation of a retinoic acid biosynthesis and signaling gene signature. We show that one such target gene, *ALDH1A1,* which regulates a key step in retinoic acid biosynthesis, is consistently upregulated with PBRM1 loss in ccRCC cell lines and primary tumors, as well as non-malignant cells. We further find that ALDH1A1 increases the tumorigenic potential of ccRCC cells. Using biochemical methods, we show that ARID2 remains bound to other PBAF subunits after loss of PBRM1 and is essential for increased ALDH1A1 after loss of PBRM1, whereas other core SWI/SNF components are dispensable, including the ATPase subunit BRG1. In total, this study uses global epigenomic approaches to uncover novel mechanisms of PBRM1 tumor suppression in ccRCC.

Introduction

The chromatin state of a cell is governed by a variety of mechanisms, including DNA methylation, histone variant incorporation, histone post-translational modification, and ATP-dependent chromatin remodeling[1]. Aberrant activation or dysfunction of any of these

Correspondence should be addressed to: Ramon Parsons, Icahn (East) Building Floor 1 Room L15C, 1425 Madison Ave., New York, NY 10029; (212) 659-5602; ramon.parsons@mssm.edu.

* These authors contributed equally to this study.

Conflict of Interest Statement:

Ramon Parsons is a co-founder of, owns equity in, receives royalty from, and serves on the scientific advisory board of Therapten Inc. Ramon Parsons also receives royalty payments from Cullgen Inc. None of the other authors declare any financial disclosures or conflicts of interest.

processes can play a role in malignant transformation. SWI/SNF complexes are one class of ATP-dependent chromatin remodelers. Cancer sequencing studies have revealed that numerous SWI/SNF subunits of the BAF and PBAF complexes are frequently mutated in human malignancies. Surveys of cancer exome sequencing studies indicate that components of these complexes are mutated in approximately 20% of all cancers[2].

The core BAF complex consists of one of two mutually exclusive ATPase subunits: either BRG1 (SMARCA4) or BRM1 (SMARCA2), in complex with SNF5 (SMARCB1), BAF155, and BAF170[3]. BRG1-containing complexes can be further divided based on their accessory subunits: ARID1A or ARID1B define the BAF complex, while PBRM1, ARID2, and BRD7 are found exclusively in the PBAF complex[4,5]. A third major SWI/SNF complex, termed the GBAF or non-canonical BAF complex, has also been recently identified that incorporates GLTSCR1 or GLTSCR1L in place of an ARID protein, and contains BRD9, but lacks the core canonical BAF subunits BAF45, SNF5, and BAF57[6].

PBRM1, also known as BAF180, Polybromo, or PB1, contains six bromodomains and two bromo-adjacent homology domains and is one of the defining subunits of the PBAF complex. We initially identified *PBRM1* as a tumor suppressor in breast cancer, with a frequency of mutation of approximately 4% in cell lines and primary tumors with loss of heterozygosity[7]. A subsequent exome sequencing study in clear cell renal cell carcinoma (ccRCC) revealed *PBRM1* mutations in 41% of tumors, making it the second most highly mutated gene in ccRCC after *VHL*[8]. Additional efforts by The Cancer Genome Atlas (TCGA) and others have found similar rates of *PBRM1* mutation in ccRCC[9,10]. Other studies have found recurrent *PBRM1* mutations in other cancer types, including pancreatic ductal adenocarcinoma (10%), intrahepatic cholangiocarcinoma (13%), gallbladder carcinoma (25%), bladder urothelial carcinoma (9%), and gastric adenocarcinoma (7%)[11–14].

The molecular basis for PBRM1 tumor suppressor function has been attributed to its ability to induce p21 and inhibit activation of S-phase gene expression, as well as its role in maintaining chromosome stability[7,8,15,16]. PBRM1 is also capable of recognizing activated p53 to help induce p21 and other p53-target genes[17]. Other work has shown that PBRM1 loss in ccRCC amplifies the HIF pathway to promote tumorigenesis in conjunction with VHL inactivation[18]. Amplification of the transcriptional outputs of HIF1, as well as STAT3, was also seen in a mouse model with dual loss of *Vhl* and *Pbrm1*[19]. This, along with other mouse studies, confirmed Pbrm1's role as a *bona fide* tumor suppressor in ccRCC[20,21]. One of these studies additionally showed that *Pbrm1* loss rescued cells from *Vhl*-loss induced replication stress to promote carcinogenesis[21]. Much recent work has focused on PBRM1's effects on the immune system and response to immunotherapy, although PBRM1's role here remains unsettled, with conflicting findings suggesting that PBRM1 deficiency can be either immunosuppressive or pro-inflammatory[22–24].

Here, we perform epigenomic and gene expression profiling to identify and then functionally validate novel cancer-related genes and pathways regulated by PBRM1 in ccRCC. We also use biochemical methods to further explore how PBRM1 loss affects PBAF complex formation. We find that loss of PBRM1 leads to increased H3K4me3 peaks

at promotors of genes associated with retinoic acid biosynthesis and signaling, leading to transcriptional activation. We functionally validate one such target gene, the aldehyde dehydrogenase *ALDH1A1,* whose expression is consistently increased in ccRCC cell lines and primary tumors with PBRM1 loss and enhances ccRCC tumor cell growth in multiple different assays *in vitro*. ARID2 positively regulates ALDH1A1 in the setting of PBRM1 deficiency, whereas other core SWI/SNF components are dispensable, including the ATPase subunit BRG1. In total, this study reveals novel mechanisms of tumor suppression by PBRM1 in ccRCC.

Materials and methods

Cell lines.

786-O (RRID:CVCL_1051), A-704 (RRID:CVCL_1065), and ACHN (RRID:CVCL_1067) cell lines were purchased from the ATCC (which authenticates cell lines using several methods, including DNA fingerprinting) in 2010–2011. MEFs were generated using standard protocols from *Pbrm1* fl/fl mice produced in our laboratory (2012–2014). Cell lines were clear of *Mycoplasma* as determined by the Lonza kit (LT07–418) within 6 months of their use. Cell lines were further authenticated in 2015 by LabCorp using a short tandem repeat method. Experiments with cancer cell lines were performed from passages 5–12. Early passage MEFs were used (<6 passages). Culturing conditions were as specified by the ATCC, unless otherwise noted.

Cell line reagents.

When treated with EGF (AF-100–15, Peprotech), the cells were starved for 16 hours in the appropriate media without FBS before treatment. Erlotinib was purchased from Fisher (#50–148-625), and DEAB (dissolved in 95% ethanol) provided in the ALDEFLUOR kit (STEMCELL, RRID:SCR_013642) was used.

Plasmids and constructs.

Full-length PBRM1 was cloned into a pBABEpuro vector. A C-terminal V5 tag was added to this plasmid using site-directed mutagenesis, and this plasmid was then used as a template to make the *PBRM1* cancer mutants. The ALDH1A1-HA vector in pcDNA was purchased from Addgene (#11610, RRID:Addgene_11610).

Xenografts.

Cells used for xenograft experiments had been split a few days prior to use and were healthy looking and still growing. 2 hr prior to injection, the cells were re-fed. They were then trypsinized, counted, washed in media, resuspended in cold media, and then combined 1:1 with cold Matrigel (Trevigen) to a concentration of 1×10^6 per 0.2 mL and kept on ice. 6-week-old female athymic nude mice were subcutaneously injected on their ventral flanks with 1×10^6 786-O control and PBRM1 shRNA cells (opposite flanks of the same mouse). Tumor xenograft growth was monitored, and after the tumors were palpable (10 days), size was measured using calipers (length and width measurements were taken, and volume calculated using the formula: (length x width^2)/2). When tumor size exceeded the limitations specified by IACUC (>1000mm^3), the mice were euthanized. These studies were approved

by the IACUC, and all mice were treated humanely according to the guidelines established by IACUC.

ALDEFLUOR assay.

The ALDEFLUOR assay kit was purchased from STEMCELL Technologies (RRID:SCR_013642), and the manufacturer's instructions were followed. Please see the Supplementary Information for a more detailed protocol.

Tumorsphere assay.

Healthy, growing cells were trypsinized, counted, and washed in tumorsphere media (appropriate cell culture medium, penicillin, streptomycin, 1x B-27 Supplement (Gibco, #17504–044), 20 ng/mL EGF, and 20 ng/mL bFGF (R&D, #233-FB-025)). Cells were then resuspended to single-cell suspensions in tumorsphere media, and 4×10^3 cells in 3 mL were plated into wells of ultra-low attachment 6-well plates (Costar, #3741). When drug treatments were added, they were added to the single-cell suspensions with mixing before plating. Tumorsphere formation was quantified after 3.5 days using phase contrast images at 100x of all cells in a well and analyzing the images with ImageJ software. A grouping of cells was counted as a tumorsphere if it was >50 μm in diameter, and represented a solid mass of cells, with indistinguishable cell borders. To measure tumorsphere self-renewal, the tumorspheres were passaged at this point. All the media was collected from a well, the cells were briefly spun down, and then resuspended in tumorsphere media and counted. Cells were re-plated as before at roughly the same starting density (e.g., 4×10^3 cells in 3 mL) – if the total cell count for a well was less than 6×10^3 cells, all the cells went back into a single well, but if the cell count was higher, the cells were divided into 2 wells. When tumorsphere formation was quantified for these cells, tumorspheres from cells that had been divided between two wells were added together. For siRNA experiments, cells were transfected with the indicated siRNA for 24 hr before they were plated for the tumorsphere assay. For the ALDH1A1 overexpression experiment, the cells were transfected for 36 hr prior to plating. Extra cells that were not plated were spun down, combined with 2X sample buffer, and then analyzed by Western Blot analysis to check for successful knockdown or overexpression.

Nuclear extraction.

Nuclear extraction was performed on 786-O and A-704 cells prior to the immunoprecipitation and glycerol gradient experiments. For each cell line, five 15 cm plates (80–90% confluent) were collected at once. Each plate was washed 2x in cold PBS, and then was collected by scraping into cold PBS containing protease inhibitors (Sigma, P8340). Cells were spun at 700xg at 4°C for 5 min. The pellet was then resuspended by pipetting and vortexing in 3.5 mL of cold Buffer A (10 mM HEPES-KOH pH 7.9, 10 mM KCl, 0.1mM EDTA, 0.1 mM EGTA), supplemented with fresh dithiothreitol (DTT) at 1 mM and protease inhibitors. After 5 min, 10% Triton X-100 in Buffer A (pre-made) was added 1:20 to a final concentration of 0.5%, and the sample was vortexed again. After another 5 min, the sample was centrifuged at 1000xg at 4°C for 5 min. The pellet (nuclei) was then washed once by resuspending in 1 mL of cold Buffer D (20 mM HEPES-KOH pH 7.9, 1 mM EDTA, 1 mM EGTA), supplemented with fresh 1 mM DTT and protease inhibitors. The sample was centrifuged again at 1000xg at 4°C for 5 min, and the pellet was now resuspended

in 0.5mL of cold Buffer C (20mM HEPES-KOH pH 7.9, 400 mM NaCl, 1 mM EDTA, 1 mM EGTA), supplemented with fresh 1 mM DTT, protease inhibitors, and 1 mM sodium orthovanadate. The sample was vortexed, passed numerous times through an 18.5G syringe, and then incubated on ice for 5 min. 10% Triton X-100 in Buffer C (pre-made) was added 1:20 to a final concentration of 0.5%, and the sample was again vortexed, passed numerous times through an 18.5G syringe, and then incubated on ice for 5 min. The sample was then centrifuged at 14,000 rpm at 4°C for 10 min. The supernatant (nuclear extract) was removed, and the extraction was repeated on the pellet, beginning with resuspension in 0.5 mL of Buffer C. The second nuclear fraction was then combined with the first, and then 0.6 volumes of cold Buffer D, supplemented with fresh 1 mM DTT and protease inhibitors, was added to lower the solute concentration. The nuclear extract was then filtered through a 0.22 μm filter using a 1 mL syringe, a small aliquot was set aside to quantify the protein concentration using the Bradford protein assay, and the nuclear extract was snap frozen and stored at −80°C.

Immunoprecipitation.

Immunoprecipitation (IP) experiments were performed on isolated nuclear extracts. 0.5 mg of nuclear extract was diluted to 1 mL total volume using cold Buffer C/D (1.0:0.6 ratio), supplemented with fresh 1 mM DTT, protease inhibitors, and 1 mM sodium orthovanadate. The nuclear extract was pre-cleared with 30 μl Protein G Dynabeads (ThermoFisher) for 1 hr at 4°C. The IP step was performed overnight at 4°C using 3 μg of targeting antibody (BRG1 (G-7) (Santa Cruz, sc-17796, RRID:AB_626762) or ARID2 (E-3) (Santa Cruz, sc-166117, RRID:AB_2060382)) or mouse IgG (Santa Cruz, #sc-2025, RRID:AB_737182) prebound to 30 μl Protein G Dynabeads. The beads were washed on a magnet 4x with 1 mL cold Buffer C/D, supplemented with fresh 1 mM DTT, protease inhibitors, and 1 mM sodium orthovanadate. After the last wash, the beads were resuspended in 60 μl of 2X sample buffer, boiled for 5 min, and then subjected to Western blot analysis. The V5 IP experiments in the A-704 lines were performed similarly, except 50 μl V5-agarose affinity gel (Sigma, A7345, RRID:AB_10062721) was used for the IP step, and 50 μl of protein A/G agarose beads (Santa Cruz, #sc-2003, RRID:AB_10201400) and 4 μg mouse IgG were used for the pre-clear step.

Glycerol gradient fractionation.

Glycerol gradients were made using 10% and 30% glycerol solutions, to a total volume of 11.5 mL per gradient, using a dual piston gradient maker (Jule, J17) and 13.2 mL thin-wall polypropylene tubes (Beckman Coulter, 14×89mm, #331372). Glycerol solutions were made by diluting glycerol (v/v) into Buffer C/D (1.0:0.6), supplemented with fresh 1 mM DTT, protease inhibitors, and 1 mM sodium orthovanadate (Buffer C – 20 mM HEPES-KOH pH 7.9, 400 mM NaCl, 1 mM EDTA, 1 mM EGTA; Buffer D – 20 mM HEPES-KOH pH 7.9, 1 mM EDTA, 1 mM EGTA). The fractionation was performed on isolated nuclear extracts diluted to a final concentration of 1.7 mg/mL in cold Buffer C/D (1.0:0.6), supplemented with fresh 1 mM DTT, protease inhibitors, and 1 mM sodium orthovanadate. 0.5 mL of the diluted nuclear extract was carefully layered on top of the glycerol gradient. The gradients were spun for 18 hr in a TH-640 swinging bucket rotor at 40,700 rpm at 4°C in an ultracentrifuge. ~0.5mL fractions (9 drops) were collected from the bottom (heavier

fractions) of the tube (24 fractions total). Aliquots of the fractions were combined with 2X sample buffer and subjected to Western blot analysis.

Microarray expression analysis.

After infection with adenovirus, MEFs were passaged 3 times, and total RNA was collected for microarray analysis using the Qiagen RNeasy kit. The Ambion WT Expression Kit (#4411973) was used to generate amplified sense-strand cDNA, and fragmentation and labeling was performed with the GeneChip WT Terminal Labeling and Controls Kit (Affymetrix, #901525). Microarray expression analysis was performed using GeneChip Mouse Gene 2.0 ST Arrays (Affymetrix, #902118) following the manufacturer's instructions.

RNA-seq.

Before RNA collection, cells were passaged and grown at the specified serum levels for 48 hours. Total RNA was collected from healthy cells that were ~70% confluent using the Qiagen RNeasy kit. Poly-A selection of mRNA, RNA-seq library preparation, and 100 base-pair single-end sequencing using an Illumina HiSeq machine were performed. FastQC (RRID:SCR_014583) checks were done on the raw data, and salmon (RRID:SCR_017036) was used to align the reads to the hg38 transcriptome and check for differential expression following previously described methods[25]. Salmon output (quant.sf files) were input directly into DESEQ2 (RRID:SCR_015687) for differential gene expression analysis[26]. A TPM cutoff of 2 was used to identify expressed genes. Differentially expressed genes were visualized in GSEA (RRID:SCR_003199) and Enrichr (RRID:SCR_001575) for pathway analysis[27].

Native ChIP-seq of histone marks.

Native ChIP-seq was performed according to well-established, published protocols[28]. Briefly, 20–50×10^6 cells were swelled and lysed using 0.1% IGEPAL, nuclei were collected by centrifugation through a sucrose gradient, and micrococcal nuclease digestion was optimized for each cell collection to primarily generate mononucleosomes, without overdigesting. For the ChIP step, 3 μg of each histone mark antibody was used, and 50 μg of chromatin was used for methyl marks, and 100 μg was used for acetyl marks. The cells were precleared by adding 30 μl of Magna ChIP Protein A+G Magnetic Beads (Millipore, #16–663) and nutating at 4°C for 20 min. The beads were removed, and 1% of the sample was removed and stored at −80°C as the input DNA, and the antibody incubation was performed overnight. 50 μl of Magna beads were then added, and a further 3 hr incubation at 4°C was carried out. Bead washing, processing of input DNA, and extraction and purification of DNA was performed per well-established published protocols, as above.

ChIP-seq library preparation and sequencing.—ChIP-seq libraries were made following well-established protocols. Briefly, 2–10 ng of DNA was end-repaired, an A-overhang was added, Illumina Truseq adapters were ligated, and DNA was run on an agarose gel and size-selected at 300–400 bp using the Qiagen Gel Extraction Kit to exclude polynucleosomes. Libraries were PCR amplified for 10–14 cycles using KAPA Biosystems HiFi PCR Master Mix. Where not indicated, all library preparation steps involved New

England Biolabs enzymes. The quality and concentration of the prepared libraries were assessed on a Bioanalyzer – the amplified libraries produced sharp peaks of ~280 bp. 75 bp single-end sequencing was performed on an Illumina NextSeq 500 machine.

ChIP-seq data processing and analysis.

Adapter sequences were removed from reads using Cutadapt (RRID:SCR_011841). Reads were mapped to the hg19 human genome using bowtie (RRID:SCR_005476). Duplicate reads were removed using samtools (RRID:SCR_002105). Matching input control was used to call peaks. Peak calling was performed using MACS2 (RRID:SCR_013291). A *P*-value cutoff of 10^{-10} was used for peak calling. Bigwig tracks were generated using deepTools (RRID:SCR_016366) bamCoverage with RPKM normalization. H3K4me3 ChIP-seq tracks were promoter normalized prior to direct comparison. Blacklisted regions (Duke_Hg19SignalRepeatArtifactRegions.bed, downloaded from the Broad Institute) were excluded from called peaks using bedtools (RRID:SCR_006646). Summary plots (metagenes) and heatmaps were generated using deepTools computeMatrix with either plotProfile or plotHeatmap.

ATAC-seq.

For all ATAC-seq libraries, 150,000 cells were harvested, tagmented with 5 μL Nextera Tn5 Transposes from the Nextera kit (Illumina) for 30 min, amplified up to 13 cycles and purified essentially as described[29]. Purified libraries were then size selected on 2% agarose gels (150–700bp). Libraries were sequenced on an Illumina Hi-Seq2500 (40 bp paired-end). Reads were trimmed for Illumina adapter sequences using in-house scripts and aligned to the GRCh37/hg19 using Bowtie2 (version 2.1.0) with parameters –S –X 2000. Reads that align to mtDNA, with quality value Q<30, as well as duplicated reads, were discarded using in-house scripts and Samtools. Coverage tracks were generated using deepTools bamCoverage with parameters –normalizeUsingRPKM. Tracks were further promoter normalized prior to direct comparison.

Statistical analysis.

Statistical analysis was performed on GraphPad Prism 8 software. Statistical tests used for specific experiments are described in the figure legends. In general, $P<0.05$ was considered significant.

Data and material availability:

Histone modification ChIP-seq, RNA-seq, ATAC-seq, and microarray datasets generated in this study are deposited at the NCBI Gene Expression Omnibus under the accession GSE102807. Any materials are available from the corresponding author upon reasonable request. RNA-seq data from previously published primary ccRCC tumors were accessed under the accession GSE86095[30].

Other experiments.

Further detailed methods can be found in the Supplementary Information.

Results

PBRM1 deficiency in ccRCC cell lines increases tumorigenic potential

To investigate PBRM1 function, we manipulated its expression in three ccRCC cell lines. We transduced 786-O cells, which are *PBRM1* wildtype and *VHL* null, with two independent and non-overlapping short hairpin RNAs (shRNAs) or with a non-targeting control shRNA[8]. PBRM1 shRNAs reduced PBRM1 protein levels by approximately 90% (Figure 1A). We also used shRNA to knock down PBRM1 protein levels in the ACHN cell line (Figure S1A). ACHN harbors a heterozygous nonsense mutation of *PBRM1* (and wildtype *VHL*); however, it has near-normal levels of wildtype PBRM1 protein[8]. We also transduced A-704 cells, which harbor a homozygous truncating mutation of *PBRM1* with mutant *VHL,* with either an empty-vector containing retrovirus (EV) or a retrovirus containing wildtype PBRM1 with a C-terminal V5 tag (WT). PBRM1 expression was stable over time in the A-704 WT cells, and no PBRM1 expression was detectable in the EV line (Figure 1B). We next compared the growth rates of these cell lines. Under normal culture conditions (media containing 10% fetal bovine serum [FBS]), the growth rates between PBRM1-deficient and PBRM1-expressing cell lines were not obviously different (Figure S1B–C). However, under reduced serum conditions, PBRM1-deficient cells grew significantly faster than PBRM1-expressing control cells, as expected (Figure 1C–D, S1C)[18].

We then performed a series of 3D growth assays to test how PBRM1 deficiency affects a hallmark of tumorigenic potential. In both 786-O and ACHN cells, PBRM1 knockdown significantly increased colony formation in soft agar (Figure 1E, S1D). A-704 EV and WT cells were unable to form colonies in soft agar. We next tested whether PBRM1 deficiency in 786-O cells increased tumorsphere-forming capacity, which is thought to represent a good surrogate measure of *in vivo* tumorigenicity. PBRM1 knockdown significantly increased the ability of 786-O cells to form free-floating tumorspheres (Figure 1F, left panel), and these cells maintained a substantially higher sphere-forming capacity after passaging (Figure 1F, right panel), indicating a higher self-renewal rate. Representative tumorsphere images are shown in Figure S1E. There were also significantly more PBRM1 shRNA cells present at the time of passage, indicating that increased tumorsphere formation was not just due to increased association of individual cells (Figure S1F).

To further test the 3D growth capacity of PBRM1 knockdown cells, we performed tumor xenograft experiments. 786-O PBRM1 shRNA cells grew significantly faster than control cells (Figure 1G) and formed significantly larger tumors (Figure S1G). Protein extracted from the tumors confirmed that PBRM1 knockdown persisted during the xenograft experiment (Figure S1H).

Since prior reports have shown that PBRM1 helps regulate p21 expression and that this is an important mechanism of tumor suppression, we also tested whether PBRM1 knockdown affects p21 induction in response to doxorubicin treatment[7]. In both the 786-O and ACHN lines, PBRM1 knockdown led to reduced induction of p21 in response to doxorubicin treatment (Figure S1I–J).

Based on the differential sensitivity to serum conditions that we observed, we hypothesized that PBRM1 may act to restrain growth factor signaling. Prior work in *Drosophila melanogaster* has demonstrated genetic antagonism between the PBAF homologous pbap complex and the EGFR pathway, and a more recent study using CRISPR and shRNA screens identified PBRM1 loss as attenuating EGFR inhibition by sustaining AKT signaling in a non-small cell lung cancer model[31,32]. Given these findings and the central role of the EGF pathway in cancer cell growth, we investigated the relationship between PBRM1 and EGF signaling further.

Before doing so, we created additional stable A-704 lines that expressed cancer-associated mutant versions of PBRM1 previously identified to have deleterious effects on function (p.T232P, p.A597D, and p.H1204P), and one in-frame deletion (p.M1209_E1214delMFYKKE, termed “6AAD”)[8]. We were unable to detect expression of the A597D mutant, and the 6AAD mutant was expressed at very low levels compared to WT (Figure S2A). On the other hand, the H1204P mutant expressed at comparable levels to the WT protein, while the T232P mutant was detectable, although at lower levels than the WT protein. Immunoprecipitation (IP) experiments indicated that the WT, H1204P, and T232P proteins bound to other PBAF subunits (Figure S2B). For these reasons, we decided to use the H1204P and T232P mutant cells in follow-up experiments.

In the cell lines we created, loss of PBRM1 heightened sensitivity to EGF stimulation (Figure S2C–F). At baseline, the 786-O PBRM1 knockdown cells had higher total EGFR levels (Figure S2C, quantified in S2E). These cells were also more sensitive to EGF stimulation (10 ng/mL) compared to the control cells as demonstrated by increased elevation of p-EGFR (Y1143), p-AKT (T308 and S473), and p-ERK levels. At 20 ng/mL EGF, p-EGFR and p-ERK levels, but not p-AKT, remained relatively elevated in the PBRM1 knockdown lines. In A-704 cells, similar trends were evident (Figure S2D, quantified in S2F). At baseline, expression of WT PBRM1 resulted in lower total EGFR levels compared to the EV control or PBRM1 mutant lines, particularly the T232P mutant. When stimulated with EGF, the WT line responded with relatively lower levels of p-EGFR (Y1173) and p-AKT (compared to all other lines at T308; only relative to the mutant lines at S473), although p-ERK levels were similar.

Next, we hypothesized that PBRM1 status would affect the growth response to EGF. In 786-O cells at very low serum, PBRM1 knockdown led to heightened growth after EGF stimulation, whereas the control cells did not respond (Figure S2G). In A-704 cells at very low serum, EGF stimulation produced divergent outcomes: the EV line responded with a slight growth increase, while EGF stimulation had a growth inhibitory effect on the WT line (Figure S2H), a phenomenon that is seen in some cell lines, including sometimes for ccRCC[33,34].

In showing heightened sensitivity to EGF stimulation and increased AKT signaling with PBRM1 loss, our findings agree with the prior study in lung cancer cells[32]. While loss of PBRM1 in this lung cancer model did not lead to an increase in the total level of EGFR or downstream ERK signaling, loss of other SWI/SNF subunits in different lung cancer models has produced these changes and thus may reflect context-dependent effects[35].

We also explored whether PBRM1 knockdown influences sensitivity to EGFR inhibition using the drug erlotinib. Having established that PBRM1 knockdown has particularly large effects on 3D growth, we tested how EGFR inhibition affected colony growth in soft-agar in 786-O cells. When treated with an intermediate dose of erlotinib (1 μM), the control cells almost completely lost their ability to form colonies, while the PBRM1 knockdown cells still formed significantly more colonies, albeit at a reduced level (Fig. S2I). At a higher dose of erlotinib (10 μM), colony growth was severely limited in both lines.

PBRM1 loss results in gained H3K4me3 peaks independently of open chromatin

As mutations of SWI/SNF subunits have previously been linked to changes in the histone modification landscape, we next performed native chromatin immunoprecipitation with next-generation sequencing (ChIP-seq) probing for H3K4me3, H3K4me1, H3K27me3, and H3K9ac in both 786-O PBRM1 shRNA as well as non-targeting control shRNA cells at normal serum conditions (10% FBS). We also performed assay for transposase accessible chromatin with next generation sequencing (ATAC-seq) and RNA sequencing (RNA-seq) in the same samples for an integrative multi-omics approach to probe the impact of PBRM1 loss on the epigenome.

We observed a notable gain of H3K4me3 peaks, a marker of active and poised promoters, in the PBRM1 knockdown lines compared to the control line. Across the two PBRM1 shRNA and the non-targeting control lines, we called 16,525 high confidence H3K4me3 peaks. We identified 1,420 (8.6%) H3K4me3 peaks as gained with knockdown of PBRM1 (average shPBRM1 $\log_2$ fold change >1) (Figure 2A–B). Conversely, only 259 (1.6%) of H3K4me3 peaks were lost with knockdown of PBRM1 (average shPBRM1 $\log_2$ fold change <−1) (Figure 2A). We did not observe widespread changes in the other histone marks (H3K9ac, H3K4me1, and H3K27me3).

After we identified the H3K4me3 landscape as most affected by knockdown of PBRM1, we next aimed to characterize the putative upstream transcription factors involved in regulation of the 1,420 gained H3K4me3 peaks. We performed ATAC-seq analysis on the 786-O lines and identified open chromatin regions within gained H3K4me3 peaks in PBRM1 knockdown cells and performed TRAP motif analysis[36]. The most highly enriched transcription factor motif was for the AP1 complex, followed by hepatocyte nuclear factor 1 beta (HNF1B), which is essential for renal development, as well as hepatocyte nuclear factor 1 alpha (HNF1A) (Figure 2C)[37]. Motif analysis was also notable for enrichment for NFE2L2 (also known as NRF2), a major regulator of cytoprotective responses to oxidative stress, including regeneration of NADPH (Figure 2C)[38].

We further assessed whether knockdown of PBRM1 resulted in open chromatin changes that could explain the observed gained H3K4me3 peaks. We integrated the sample-matched ATAC-seq datasets and performed metagene analysis comparing open chromatin levels in PBRM1 shRNA versus control cells at the loci of gained or lost H3K4me3 peaks (Figure 2D). We found the level of ATAC-seq reads to be comparable at these H3K4me3 peaks regardless of PBRM1 status. This finding suggests that the differences in H3K4me3 levels may be independent of changes in open chromatin, which has been noted previously for other histone modifications in cancer[39]. In addition, we performed a global analysis to

look for differences in the open chromatin landscape between PBRM1 shRNA and control 786-O cells. We called a total of 56,826 high confidence ATAC-seq peaks and identified 501 peaks (0.88%) as gained and 646 peaks (1.1%) as lost following knockdown of PBRM1 (absolute $\log_2$ fold change >1). Taken together, our data suggest PBRM1 deficiency does not profoundly impact the open chromatin landscape of ccRCC, reproducing observations made by other groups[18].

We next sought to characterize downstream transcriptional programs activated by the altered H3K4me3 peaks. Gained and lost H3K4me3 peaks correlated with mRNA expression changes in sample-matched RNA-seq datasets (Figure 3A). We then derived a gene signature for gained H3K4me3 peaks in PBRM1 deficiency by associating the 1,420 gained peaks with genes based on the closest transcriptional start site, filtering by genes up-regulated in PBRM1 shRNA cells over non-targeting controls ($P_{adj} < 0.05$, $\log_2$ fold change > 1).

We subjected this gene signature to pathway analysis using Enrichr[40]. The most significantly enriched pathway using the KEGG database was retinol metabolism (P_{adj} = 3.7e-4) (Figure 3B). We validated this observation using an alternative database (Reactome), similarly finding retinoic acid metabolism biosynthesis (P_{adj} = 0.006) and signaling (P_{adj} = 0.017) as the second and fourth most significantly enriched pathways, respectively, associated with gained H3K4me3 peaks in PBRM1 shRNA cells (Figure 3C).

Cellular production of retinoic acid is tightly regulated[41]. Generating the functionally active hormone retinoic acid first requires synthesis of its relatively inactive precursor, retinol, a vitamin A compound. Retinol dehydrogenases convert retinol to retinaldehyde, which becomes irreversibly converted to retinoic acid by retinaldehyde dehydrogenases. Increased retinaldehyde dehydrogenase activity induces upstream retinaldehyde reductases, which convert retinaldehyde back to retinol to maintain homeostasis, although with weak catalytic activity and modest effects on retinoic acid production in some contexts[42]. While *Pbrm1* has previously been linked to retinoic acid-dependent gene activation in mouse cardiac development, to our knowledge, an association between PBRM1 loss in ccRCC and retinoic acid metabolism and signaling has not previously been described in the literature[43].

We next looked at H3K4me3 levels and expression changes at specific genes involved in retinoic acid biosynthesis and enriched in our gene signature. We observed robust increased H3K4me3 deposition at the promoter of the retinaldehyde dehydrogenase *ALDH1A1* following knockdown of PBRM1 in 786-O cells (Figure 3D). This corresponded with increased RNA-seq expression of *ALDH1A1* in these cells, at both 10% and 1% FBS (Figure 3E).

In addition, we observed increased H3K4me3 and RNA-seq expression of the retinaldehyde reductase *DHRS3*, as well as the retinol dehydrogenases *DHRS9* and *DHRS4L2* (a splice isoform of *DHRS4*), other genes enriched in our signature, although there was some variation in expression changes between the PBRM1 shRNA lines or the FBS conditions (Figure S3A–F)[44,45]. We also identified *UGT1A8*, a UDP-glucuronosyltransferase involved in retinoic acid metabolism, as up-regulated as part of our signature (Figure S3G–H)[46]. We additionally looked at the degree of open chromatin at the loci of these genes but did not see

significant differences between the PBRM1 shRNA and control cells, in accordance with our global analysis (Figure S3I).

PBRM1 deficiency results in higher ALDH1A1 expression which increases tumorsphere growth

Having identified a possible role for PBRM1 in regulating retinoic acid biosynthesis and signaling in ccRCC, we next sought to clarify how PBRM1 loss affected one of the key enzymes in this pathway: ALDH1A1. ALDH1A1 (also known as aldehyde dehydrogenase 1 or retinaldehyde dehydrogenase 1) is one of a class of oxidizing enzymes that convert aldehydes to carboxylic acids[47]. It is part of the retinoic acid metabolic pathway and irreversibly converts retinaldehyde to retinoic acid. Aldehyde dehydrogenases (ALDHs) also protect against oxidative stress and UV damage and help catalyze the breakdown of lipid peroxides by serving as aldehyde scavengers[48]. ALDH1A1 participates in hematopoietic stem cell development, white versus brown fat programming, insulin signaling, and GABA synthesis[49–52]. It has also been identified as a marker of tumor-initiating cells or cancer stem cells in a variety of cancer types[53,54].

We used quantitative reverse transcription polymerase chain reaction (qRT-PCR) to confirm that *ALDH1A1* mRNA levels increase with PBRM1 deficiency in the 786-O cells and decrease with PBRM1 expression in A-704 cells (Figure S4A). We next asked whether ALDH1A1 protein levels change accordingly. In 786-O and ACHN cells, ALDH1A1 protein increased with PBRM1 knockdown (Figure 4A and S4B). In A-704 cells, expression of WT PBRM1, but not the mutated forms, resulted in lower ALDH1A1 protein levels (Figure 4B). Additionally, in the immortalized breast line MCF10A, ALDH1A1 protein increased with stable knockdown of PBRM1 (Figure S4C), suggesting that PBRM1 regulation of ALDH1A1 may not be restricted to the malignant setting.

To further investigate this, we isolated murine embryonic fibroblasts (MEFs) from conditional *Pbrm1* mice we generated, where Cre-mediated recombination would cause a frame-shift mutation of the *Pbrm1* allele. Western blot analysis indicated effective recombination and loss of Pbrm1 expression in MEFs infected with adenovirus expressing Cre-recombinase (Fig. S4D). We then used microarrays to perform expression analysis on three matched sets of MEFs with or without Pbrm1 expression. *Aldh1a1* was among the top 50 most-altered genes in the MEFs (Fig. S4E). We confirmed increased *Aldh1a1* mRNA expression with *Pbrm1* loss using qRT-PCR (Figure S4F).

Additionally, we used the ALDEFLUOR assay to measure ALDH1-class enzyme activity in the 786-O and A-704 lines[55]. The results mirrored those seen for ALDH1A1 protein levels: PBRM1 knockdown in 786-O cells increased the ALDEFLUOR-positive cell population by approximately 50%, while WT PBRM1 expression in A-704 cells decreased the ALDEFLUOR-positive population by approximately 33%, and the cancer mutants had no impact (Figure 4C–D).

To examine if *ALDH1A1* expression was altered in primary ccRCC tumors with *PBRM1* mutation, we used the publicly available ccRCC primary tumor expression dataset from the TCGA available on the cBioPortal for Cancer Genomics[56,57]. We divided the tumors

into those with *PBRM1* mutations (Mut) and those without (WT). Consistent with our cell line data, *ALDH1A1* expression was significantly increased in the *PBRM1* mutant setting (Figure S4G). Next, to discern if these expression changes were specific to *PBRM1* mutant tumors only, we divided the TCGA tumors by *SETD2* and *BAP1* mutation status and observed no correlation with *ALDH1A1* expression levels (Figure S4H–I). We also checked for differential *ALDH1A1* expression in another publicly available ccRCC expression dataset from a 2012 study that profiled *BAP1* and *PBRM1* mutant tumors and tumorgrafts[58]. *ALDH1A1* expression was significantly altered in the *PBRM1* mutant setting here as well (Figure S4J). Additionally, analyzing a previously published cohort of 10 ccRCCs, *PBRM1* mutated tumors ($n = 7$) expressed significantly higher *ALDH1A1* as compared to wildtype tumors ($n = 3$) (Figure S4K)[30].

We next investigated whether ALDH1A1 contributed to the increased 3D proliferation of PBRM1-deficient cells. Soft-agar assays in 786-O cells to which we added the ALDH-class inhibitor DEAB (which, of note, inhibits other ALDH isoenzymes in addition to ALDH1A1) revealed a dose-dependent inhibition of colony formation in PBRM1 knockdown cells (Figure 4E)[59]. At the highest dose of DEAB (15 μM), which is the dose used to set the negative baseline in the ALDEFLUOR assay, an equally low number of colonies could form for both control and PBRM1 knockdown cells. To show that these effects were not specific to the soft-agar assay, we also performed tumorsphere assays with or without high-dose (15 μM) DEAB (Figure 4F). The addition of DEAB almost completely abrogated the ability of 786-O cells to form tumorspheres, indicating that some level of ALDH-class activity is required for tumorsphere formation in both 786-O PBRM1 shRNA and control cells. Importantly, the addition of DEAB up to 100 μM did not result in cytotoxic or cytostatic effects in 2D growth analysis for either cell line, at least at the normal serum conditions used in the experiment, suggesting that ALDH-class activity may be specifically required for anchorage independent growth (Figure S4L).

To demonstrate that this effect was due to ALDH1A1 inhibition specifically, we knocked down *ALDH1A1* in 786-O cells using three different siRNAs (Figure S4M). As seen with DEAB addition, *ALDH1A1* knockdown reduced the cells' ability to form tumorspheres (Figure 4G). The level of reduction, however, was not as complete as that seen with high-dose DEAB, suggesting either incomplete *ALDH1A1* knockdown or potential compensation by other ALDH isoenzymes. There was also some variability between the *ALDH1A1* siRNA oligos in their tumorsphere-reducing capacity, suggesting possible off-target effects as well. Therefore, we also assessed whether ALDH1A1 overexpression on its own could increase tumorsphere forming capacity. Compared to an empty vector control (pcDNA-EV), ALDH1A1 overexpression (pcDNA-ALDH1A1-HA) in 786-O control cells nearly doubled the number of tumorspheres that grew (Figure 4H).

With PBRM1 deficiency, ARID2 is more highly expressed and remains bound to other SWI/SNF subunits

Given the importance of considering how remaining SWI/SNF subunits come together when one subunit is mutated, and the fact that numerous recent reports have demonstrated a synthetic lethal relationship between homologous SWI/SNF subunits, we next explored how

PBRM1 deficiency affects the levels and assembly of other PBAF subunits[60,61–64]. Western blot analysis of PBAF subunits in the 786-O and ACHN cells revealed increased ARID2 levels with PBRM1 knockdown in both shRNA lines, but not consistently increased SNF5 or BRG1 levels (Figure 5A and S5A). In the A-704 cells, expression of WT PBRM1 resulted in lower ARID2 protein levels, whereas levels remained stable with expression of the cancer-associated mutants (Figure 5B). SNF5 and BRG1 levels remained stable in all A-704 lines. Transcriptional analysis using RNA-seq in the 786-O cells and qRT-PCR analysis in the 786-O and A-704 cells showed a slight trend towards increased *ARID2* transcription in the PBRM1-deficient setting, but these changes were not significant (Figure S5B and C). However, in the previously mentioned publicly available ccRCC datasets, increased *ARID2* mRNA levels were significantly associated with *PBRM1* mutation status (Figure S5D). Overall, these findings suggest that increased ARID2 levels with PBRM1 deficiency may be at least partially transcriptional, but there are likely other contributing mechanisms.

We next investigated whether ARID2 protein was still assembling into a complex with other SWI/SNF components. BRG1 and ARID2 IP experiments revealed that ARID2 remained bound to BRG1 in the PBRM1 deficient setting (Figure 5C–D, S5E). These results are consistent with previous studies that reported PBRM1 was dispensable for the assembly of the PBAF complex[65].

These IP experiments did not preclude the possibility that ARID2 was binding to other proteins outside the PBAF complex. To determine if this was the case, we performed glycerol gradient fractionation of nuclear extracts from the 786-O cells. Based on published reports, we used a 10–30% glycerol gradient and spun for 18 hours to ensure separation of lower molecular weight complexes[60,63]. Analysis of fractions 2–24 (out of 24 total fractions) revealed that SWI/SNF subunits, including PBRM1 and ARID2, eluted only in the heavier fractions (Figure S5F). No ARDI2 was found in lighter fractions. We then looked at elution patterns at higher resolution in the heavier fractions only (Figure 5E). In the control cells, ARID2 and PBRM1 could be found in fractions 1–5, but peaked in fractions 1–2. BRG1 and SNF5 were found mostly in fractions 4–6. These results imply that the majority of ARID2 and PBRM1 is found outside the PBAF complex in the control cells. After PBRM1 knockdown, ARID2 shifted to lighter fractions, now peaking in fractions 4–5. BRG1 and SNF also shifted to slightly lighter fractions and could now be found in fractions 4–7, peaking in fraction 5. Of note, there were small differences in the elution patterns between the two PBRM1 shRNAs lines, with more SNF5 remaining in fraction 4 and ARID2 eluting in a broader range of fractions in PBRM1 shRNA #2 cells. The elution patterns of ARID2, BRG1, and SNF5 are quantified in Figure S5G. Overall, these results support the IP findings and suggest that after PBRM1 knockdown, ARID2 is bound in a PBAF-like complex that also contains BRG1 and SNF5. This complex elutes in slightly lighter fractions, perhaps reflecting the loss of PBRM1 inclusion.

Based on its domain structure containing six bromodomains capable of binding acetylated histones and the fact that it is one of the defining subunits of the PBAF complex, PBRM1 has been proposed as a targeting SWI/SNF subunit, helping direct the complex to genomic loci. Additionally, many of the *PBRM1* mutations are in the bromodomains. Because of this and our finding that a PBAF-like complex containing ARID2 remained intact after PBRM1

knockdown, we attempted to probe genomic occupancy of ARID2 with and without PBRM1 knockdown. However, we were unable to detect high-quality ARID2 ChIP-seq peaks using four commercially available antibodies in 786-O cells.

ARID2 positively regulates ALDH1A1 in the setting of PBRM1 deficiency

Based on our IP and glycerol gradient fractionation experiments, we next asked if ARID2 contributed to *ALDH1A1* regulation in the setting of PBRM1 deficiency. When we knocked down ARID2 using siRNAs in 786-O PBRM1 knockdown cells, ALDH1A1 protein expression declined significantly (Figure 6A, S6A). PBRM1 protein levels also declined after ARID2 knockdown, confirming previous findings that ARID2 is required for PBAF-complex stability[65]. The ALDH1A1 changes were confirmed to occur at the mRNA level (Figure S6B). In A-704 EV cells, ARID2 knockdown likewise decreased ALDH1A1 protein expression but not as completely as in the 786-O cells (Figure S6C). We next tested whether ARID2 knockdown affected clonal expansion via the tumorsphere assay. With ARID2 knockdown, the tumorsphere forming capacity significantly declined for 786-O cells (Figure 6B, S6D). The results resembled the effects of knocking down or inhibiting ALDH1A1.

We also tested whether other PBAF subunits were required for ALDH1A1 upregulation with PBRM1 deficiency. We knocked down SNF5 or BRG1 using siRNAs in 786-O cells (Figure 6C–D). However, unlike ARID2, SNF5 and BRG1 were dispensable for the high levels of ALDH1A1 expression in the PBRM1 knockdown line. We also performed the SNF5 knockdown in the A-704 lines (Figure S6E). In the EV cells, SNF5 knockdown led to an increase in ALDH1A1 expression, while in the WT cells, no ALDH1A1 expression was detectable. Although the ATPase subunit BRM has not previously been reported to bind in a complex with ARID2, considering the seeming dispensability of BRG1, we wondered whether a subunit switch of BRM for BRG1 was occurring with PBRM1 deficiency. We tested this by knocking down BRM in 786-O cells, but again saw no changes in ALDH1A1 protein levels in the setting of PBRM1 knockdown (Figure S6F). To test if either ATPase subunit was required, we also performed the double knockdown of BRM and BRG1, but still saw no changes in ALDH1A1 protein expression with PBRM1 knockdown (Fig. S6G). As BRG1 knockdown did not affect ALDH1A1 protein levels in the PBRM1 knockdown cells, we next tested how BRG1 knockdown impacted tumorsphere-forming capacity. While BRG1 knockdown did not decrease tumorsphere formation, as expected given the ALDH1A1 stability in this setting, BRG1 siRNA #5 increased tumorsphere formation compared to the control siRNA in the control shRNA cells, while BRG1 siRNA #1 had a similar effect in the PBRM1 shRNA cells, suggesting possible off-targets effects from these oligos as well as ALDH1A1-independent effects on tumorsphere formation (Figure 6E, S6H).

Discussion

Based on our biochemical and ChIP-seq findings, we propose that loss of PBRM1 results in changes to the epigenomic landscape, mostly in the form of gained H3K4me3 peaks. These gained H3K4me3 peaks were notably associated with increased gene expression and enriched for a retinoic acid biosynthesis and signaling gene signature in the setting

of PBRM1 deficiency. We leveraged this signature to identify PBRM1's regulation of ALDH1A1, an aldehyde dehydrogenase that irreversibly converts retinaldehyde to retinoic acid, and found that ALDH1A1 can promote tumorigenesis in ccRCC.

In contrast to H3K4me3, other histone marks, including H3K9ac, H3K4me1, and H3K27me3, remain largely unchanged. Our integrated ATAC-seq analysis indicates that the H3K4me3 gained peaks are independent of changes in open chromatin. In fact, we did not see profound global changes in the open chromatin landscape with PBRM1 deficiency in 786-O cells, in line with a prior report looking at nucleosome positioning using MNase-seq[18]. Instead, the gain of H3K4me3 peaks may be due to the recruitment of activating transcription factors or other co-factors. Loss of PBRM1 could serve to activate methyltransferases such as MLL1 that methylate H3K4, or block demethylases such as KDM5A-C which demethylate H3K4.

Additionally, with PBRM1 depletion, we saw few changes in the H3K27me3 landscape. This suggests PBRM1 loss does not lead to heightened EZH2 methyltransferase activity that has been seen in other cancer types with SWI/SNF subunit mutations[66,67]. However, some studies have shown that EZH2 is essential in *PBRM1* mutant cancers, but that these and other SWI/SNF-mutant cancers may be primarily dependent on a non-catalytic role of EZH2 in stabilizing the PRC2 complex[68]. Our results do not preclude the possible role of non-canonical EZH2 and PRC2 functioning.

Indeed, as mentioned previously, the loss of PBRM1 did not significantly impact the open chromatin landscape, suggesting PBRM1 may be dispensable for this role in the PBAF complex. After loss of PBRM1, ARID2 still associates in a PBAF-like complex, in agreement with previous reports on PBAF complex assembly. Compatible with these assembly dynamics, we found that while ARID2 is required for PBRM1 stability, PBRM1 is dispensable for ARID2 expression. In fact, we found that ARID2 levels increase with PBRM1 deficiency, and that slightly increased *ARID2* transcription may only partially account for this change, potentially reflecting post-translational stabilization. Fractionation experiments revealed that in control 786-O cells, the majority of ARID2 and PBRM1 elute in the heaviest fractions, separate from the major peaks of BRG1 and SNF5, and thus presumably outside of the major population of the SWI/SNF complex. This is in line with a previous study of SWI/SNF fractionation patterns in mouse brain nuclear extracts that also found most of the PBRM1 eluting apart from other PBAF components in the heaviest fractions[63]. The authors conjectured that the PBRM1 in these fractions could be part of the mitotic machinery, as PBRM1 had previously been found to localize to the kinetochore during mitosis[69]. In our cells, with PBRM1 knockdown, we saw a shift in the ARID2 elution pattern away from these heavy fractions and into lighter fractions also containing BRG1 and SNF5, but not into other fractions devoid of BRG1 and SNF5. These findings suggest that PBRM1 deficiency is compensated by increased or stabilized ARID2 expression and possibly increased ARID2 association with SWI/SNF components.

Interestingly, however, while ARID2 is required for the upregulation of ALDH1A1 seen with PBRM1 deficiency and the corresponding increase in tumorigenic potential, the core PBAF subunits SNF5 and BRG1 seem dispensable. While subtle changes in the level of

open chromatin could be occurring and having impact, the seeming stability of chromatin accessibility and dispensability of the actual chromatin remodeling subunits (BRG1 and BRM) suggest that the ARID2 complex devoid of PBRM1 could be acting at least partially in more novel, uncharacterized ways to affect transcription. Of note, this does not preclude the necessity of chromatin remodeling or BRG1 for other oncogenic effects of PBRM1 loss in ccRCC, as has been seen in other studies[18]. Alternatively, the regulation of ALDH1A1 expression by ARID2 in the PBRM1-deficient setting could be explained by loss of proper functioning of the higher molecular-weight complex containing ARID2 (and potentially PBRM1) seen in the 786-O control cells. This model would also account for the chromatin accessibility and SNF, BRG1, and BRM findings. Further work is needed to better elucidate this mechanism and characterize the composition and function of the higher molecular-weight ARID2-containing complex.

We decided to further investigate PBRM1 regulation of *ALDH1A1* expression. Numerous studies have identified ALDH1A1 as a marker of tumor-initiating cells, although it is unclear if ALDH1A1 promotes tumorigenicity and how it does so. Not much is known about the regulation of ALDH1A1 expression in cancer, although recent studies have posited upregulation by β-catenin or Smad4-mediated repression in prostate cancer cells[70,71]. Another study has described inhibition of ALDH1A1 by post-translational acetylation in breast cancer cells, which is reversed by SIRT2 action downstream of NOTCH signaling[72]. Our results indicate a novel method of regulation by PBRM1. The association between *PBRM1* status and *ALDH1A1* levels was confirmed in multiple primary tumor datasets of ccRCC. The association was also seen in the immortalized breast line MCF10A, as well as MEFs where *Pbrm1* was deleted by Cre recombinase, suggesting that PBRM1 may play a role in retinoic acid homeostasis outside of the malignant setting. Additionally, our results suggest that ALDH1A1 is more than just a marker of tumor-initiating cells but can directly increase the tumorigenic potential of cells. Regulation of retinoic acid biosynthesis and signaling may also have important implications for PBRM1's role in modifying the tumor immune microenvironment. A recent study found that increased retinoic acid production by tumors because of IL-13 stimulation from the tumor microenvironment generates a more immunosuppressive microenvironment that promotes tumor immune evasion and tumor growth[73]. Regulation of ALDH1A1 by PBRM1 and ARID2 may represent an alternative or additional mechanism of modulating retinoic acid levels in the tumor microenvironment, although additional work here is needed. Overall, our data offer the intriguing possibility that targeting ALDH1A1 could be beneficial for cancer patients with *PBRM1* mutations.

Supplementary Material

Refer to Web version on PubMed Central for supplementary material.

Acknowledgements

We thank Dr. Ravi Sachidanandam and the Department of Oncological Sciences Core for performing the ChIP-seq sequencing and offering advice and guidance on analysis. We would also think to thank Asif Chowdhury from the Bernstein lab for technical advice on native histone modification ChIP-seq. We would also like to acknowledge the Transgenic Mouse Core at Columbia University for helping make the *Pbrm1* fl/fl mouse, and the Genomics Core Facility at the Department of Genetics and Genomic Sciences for performing the RNA-seq library preparation and sequencing. We thank the Steven Johnson lab for providing the ALDH1A1-HA vector through Addgene. Lastly,

we would like to acknowledge Drs. Jan Kitajewski, Wei Gu, Adolfo Ferrando, and Tom Maniatis for their helpful advice and guidance. This work was supported by the National Institutes of Health, grants R01 CA082783 (to R. Parsons), T32 GM 7367-36 (to D. Schoenfeld), U54 CA193313 (to R. Rabadan), 5TL1 TR000082 (to S. Zairis), F30CA243207 (to R. Zhou), R35CA220491 to (R. Parsons), R01CA230854 (to R. Parsons), P30CA196521 (to R. Parsons), R01CA154683 (to E. Bernstein), and R01CA218024 (to E. Bernstein).

References

1. Chen T & Dent SY Chromatin modifiers and remodellers: regulators of cellular differentiation. Nat Rev Genet 15, 93–106, doi:10.1038/nrg3607 (2014). [PubMed: 24366184]
2. Kadoch C et al. Proteomic and bioinformatic analysis of mammalian SWI/SNF complexes identifies extensive roles in human malignancy. Nat Genet 45, 592–601, doi:10.1038/ng.2628 (2013). [PubMed: 23644491]
3. Phelan ML, Sif S, Narlikar GJ & Kingston RE Reconstitution of a core chromatin remodeling complex from SWI/SNF subunits. Mol Cell 3, 247–253, doi:10.1016/s1097-2765(00)80315-9 (1999). [PubMed: 10078207]
4. Wang W et al. Purification and biochemical heterogeneity of the mammalian SWI-SNF complex. EMBO J 15, 5370–5382 (1996). [PubMed: 8895581]
5. Wilson BG & Roberts CW SWI/SNF nucleosome remodellers and cancer. Nat Rev Cancer 11, 481–492, doi:10.1038/nrc3068 (2011). [PubMed: 21654818]
6. Alpsoy A & Dykhuizen EC Glioma tumor suppressor candidate region gene 1 (GLTSCR1) and its paralog GLTSCR1-like form SWI/SNF chromatin remodeling subcomplexes. J Biol Chem 293, 3892–3903, doi:10.1074/jbc.RA117.001065 (2018). [PubMed: 29374058]
7. Xia W et al. BAF180 is a critical regulator of p21 induction and a tumor suppressor mutated in breast cancer. Cancer Res 68, 1667–1674, doi:10.1158/0008-5472.CAN-07-5276 (2008). [PubMed: 18339845]
8. Varela I et al. Exome sequencing identifies frequent mutation of the SWI/SNF complex gene PBRM1 in renal carcinoma. Nature 469, 539–542, doi:10.1038/nature09639 (2011). [PubMed: 21248752]
9. Cancer Genome Atlas Research, N. Comprehensive molecular characterization of clear cell renal cell carcinoma. Nature 499, 43–49, doi:10.1038/nature12222 (2013). [PubMed: 23792563]
10. Sato Y et al. Integrated molecular analysis of clear-cell renal cell carcinoma. Nat Genet 45, 860–867, doi:10.1038/ng.2699 (2013). [PubMed: 23797736]
11. Cancer Genome Atlas Research, N. Comprehensive molecular characterization of gastric adenocarcinoma. Nature 513, 202–209, doi:10.1038/nature13480 (2014). [PubMed: 25079317]
12. Cancer Genome Atlas Research, N. Comprehensive molecular characterization of urothelial bladder carcinoma. Nature 507, 315–322, doi:10.1038/nature12965 (2014). [PubMed: 24476821]
13. Shain AH et al. Convergent structural alterations define SWItch/Sucrose NonFermentable (SWI/SNF) chromatin remodeler as a central tumor suppressive complex in pancreatic cancer. Proc Natl Acad Sci U S A 109, E252–259, doi:10.1073/pnas.1114817109 (2012). [PubMed: 22233809]
14. Jiao Y et al. Exome sequencing identifies frequent inactivating mutations in BAP1, ARID1A and PBRM1 in intrahepatic cholangiocarcinomas. Nat Genet 45, 1470–1473, doi:10.1038/ng.2813 (2013). [PubMed: 24185509]
15. Brownlee PM, Chambers AL, Cloney R, Bianchi A & Downs JA BAF180 promotes cohesion and prevents genome instability and aneuploidy. Cell Rep 6, 973–981, doi:10.1016/j.celrep.2014.02.012 (2014). [PubMed: 24613357]
16. Kakarougkas A et al. Requirement for PBAF in transcriptional repression and repair at DNA breaks in actively transcribed regions of chromatin. Mol Cell 55, 723–732, doi:10.1016/j.molcel.2014.06.028 (2014). [PubMed: 25066234]
17. Cai W et al. PBRM1 acts as a p53 lysine-acetylation reader to suppress renal tumor growth. Nat Commun 10, 5800, doi:10.1038/s41467-019-13608-1 (2019). [PubMed: 31863007]
18. Gao W, Li W, Xiao T, Liu XS & Kaelin WG Jr. Inactivation of the PBRM1 tumor suppressor gene amplifies the HIF-response in VHL−/− clear cell renal carcinoma. Proc Natl Acad Sci U S A 114, 1027–1032, doi:10.1073/pnas.1619726114 (2017). [PubMed: 28082722]

19. Nargund AM et al. The SWI/SNF Protein PBRM1 Restrains VHL-Loss-Driven Clear Cell Renal Cell Carcinoma. Cell Rep 18, 2893–2906, doi:10.1016/j.celrep.2017.02.074 (2017). [PubMed: 28329682]
20. Gu YF et al. Modeling Renal Cell Carcinoma in Mice: Bap1 and Pbrm1 Inactivation Drive Tumor Grade. Cancer Discov 7, 900–917, doi:10.1158/2159-8290.CD-17-0292 (2017). [PubMed: 28473526]
21. Espana-Agusti J, Warren A, Chew SK, Adams DJ & Matakidou A Loss of PBRM1 rescues VHL dependent replication stress to promote renal carcinogenesis. Nat Commun 8, 2026, doi:10.1038/s41467-017-02245-1 (2017). [PubMed: 29229903]
22. Braun DA et al. Interplay of somatic alterations and immune infiltration modulates response to PD-1 blockade in advanced clear cell renal cell carcinoma. Nat Med 26, 909–918, doi:10.1038/s41591-020-0839-y (2020). [PubMed: 32472114]
23. Miao D et al. Genomic correlates of response to immune checkpoint therapies in clear cell renal cell carcinoma. Science 359, 801–806, doi:10.1126/science.aan5951 (2018). [PubMed: 29301960]
24. Liu XD et al. PBRM1 loss defines a nonimmunogenic tumor phenotype associated with checkpoint inhibitor resistance in renal carcinoma. Nat Commun 11, 2135, doi:10.1038/s41467-020-15959-6 (2020). [PubMed: 32358509]
25. Patro R, Duggal G, Love MI, Irizarry RA & Kingsford C Salmon provides fast and bias-aware quantification of transcript expression. Nat Methods 14, 417–419, doi:10.1038/nmeth.4197 (2017). [PubMed: 28263959]
26. Love MI, Huber W & Anders S Moderated estimation of fold change and dispersion for RNA-seq data with DESeq2. Genome Biol 15, 550, doi:10.1186/s13059-014-0550-8 (2014). [PubMed: 25516281]
27. Subramanian A et al. Gene set enrichment analysis: a knowledge-based approach for interpreting genome-wide expression profiles. Proc Natl Acad Sci U S A 102, 15545–15550, doi:10.1073/pnas.0506580102 (2005). [PubMed: 16199517]
28. Hasson D et al. The octamer is the major form of CENP-A nucleosomes at human centromeres. Nat Struct Mol Biol 20, 687–695, doi:10.1038/nsmb.2562 (2013). [PubMed: 23644596]
29. Fontanals-Cirera B et al. Harnessing BET Inhibitor Sensitivity Reveals AMIGO2 as a Melanoma Survival Gene. Mol Cell 68, 731–744 e739, doi:10.1016/j.molcel.2017.11.004 (2017). [PubMed: 29149598]
30. Yao X et al. VHL Deficiency Drives Enhancer Activation of Oncogenes in Clear Cell Renal Cell Carcinoma. Cancer Discov 7, 1284–1305, doi:10.1158/2159-8290.CD-17-0375 (2017). [PubMed: 28893800]
31. Rendina R, Strangi A, Avallone B & Giordano E Bap170, a subunit of the Drosophila PBAP chromatin remodeling complex, negatively regulates the EGFR signaling. Genetics 186, 167–181, doi:10.1534/genetics.110.118695 (2010). [PubMed: 20551433]
32. Liao S et al. A genetic interaction analysis identifies cancer drivers that modify EGFR dependency. Genes Dev 31, 184–196, doi:10.1101/gad.291948.116 (2017). [PubMed: 28167502]
33. Xie W, Su K, Wang D, Paterson AJ & Kudlow JE MDA468 growth inhibition by EGF is associated with the induction of the cyclin-dependent kinase inhibitor p21WAF1. Anticancer Res 17, 2627–2633 (1997). [PubMed: 9252692]
34. Ramp U et al. Functional intactness of stimulatory and inhibitory autocrine loops in human renal carcinoma cell lines of the clear cell type. J Urol 157, 2345–2350 (1997). [PubMed: 9146668]
35. Papadakis AI et al. SMARCE1 suppresses EGFR expression and controls responses to MET and ALK inhibitors in lung cancer. Cell Res 25, 445–458, doi:10.1038/cr.2015.16 (2015). [PubMed: 25656847]
36. Thomas-Chollier M et al. Transcription factor binding predictions using TRAP for the analysis of ChIP-seq data and regulatory SNPs. Nat Protoc 6, 1860–1869, doi:10.1038/nprot.2011.409 (2011). [PubMed: 22051799]
37. Clissold RL, Hamilton AJ, Hattersley AT, Ellard S & Bingham C HNF1B-associated renal and extra-renal disease-an expanding clinical spectrum. Nat Rev Nephrol 11, 102–112, doi:10.1038/nrneph.2014.232 (2015). [PubMed: 25536396]

38. Tonelli C, Chio IIC & Tuveson DA Transcriptional Regulation by Nrf2. Antioxid Redox Signal 29, 1727–1745, doi:10.1089/ars.2017.7342 (2018). [PubMed: 28899199]
39. Roe JS et al. Enhancer Reprogramming Promotes Pancreatic Cancer Metastasis. Cell 170, 875–888 e820, doi:10.1016/j.cell.2017.07.007 (2017). [PubMed: 28757253]
40. Kuleshov MV et al. Enrichr: a comprehensive gene set enrichment analysis web server 2016 update. Nucleic Acids Res 44, W90–97, doi:10.1093/nar/gkw377 (2016). [PubMed: 27141961]
41. Napoli JL Retinoic acid biosynthesis and metabolism. FASEB J 10, 993–1001, doi:10.1096/fasebj.10.9.8801182 (1996). [PubMed: 8801182]
42. Adams MK, Belyaeva OV, Wu L & Kedishvili NY The retinaldehyde reductase activity of DHRS3 is reciprocally activated by retinol dehydrogenase 10 to control retinoid homeostasis. J Biol Chem 289, 14868–14880, doi:10.1074/jbc.M114.552257 (2014). [PubMed: 24733397]
43. Wang Z et al. Polybromo protein BAF180 functions in mammalian cardiac chamber maturation. Genes Dev 18, 3106–3116, doi:10.1101/gad.1238104 (2004). [PubMed: 15601824]
44. Wang C, Kane MA & Napoli JL Multiple retinol and retinal dehydrogenases catalyze all-trans-retinoic acid biosynthesis in astrocytes. J Biol Chem 286, 6542–6553, doi:10.1074/jbc.M110.198382 (2011). [PubMed: 21138835]
45. Su ZJ et al. Bioinformatic analysis of the human DHRS4 gene cluster and a proposed mechanism for its transcriptional regulation. BMC Mol Biol 11, 43, doi:10.1186/1471-2199-11-43 (2010). [PubMed: 20525226]
46. Rowbotham SE, Illingworth NA, Daly AK, Veal GJ & Boddy AV Role of UDP-glucuronosyltransferase isoforms in 13-cis retinoic acid metabolism in humans. Drug Metab Dispos 38, 1211–1217, doi:10.1124/dmd.109.031625 (2010). [PubMed: 20308471]
47. Xu X et al. Aldehyde dehydrogenases and cancer stem cells. Cancer Lett 369, 50–57, doi:10.1016/j.canlet.2015.08.018 (2015). [PubMed: 26319899]
48. Singh S et al. Aldehyde dehydrogenases in cellular responses to oxidative/electrophilic stress. Free Radic Biol Med 56, 89–101, doi:10.1016/j.freeradbiomed.2012.11.010 (2013). [PubMed: 23195683]
49. Kim JI et al. Aldehyde dehydrogenase 1a1 mediates a GABA synthesis pathway in midbrain dopaminergic neurons. Science 350, 102–106, doi:10.1126/science.aac4690 (2015). [PubMed: 26430123]
50. Ghiaur G et al. Regulation of human hematopoietic stem cell self-renewal by the microenvironment's control of retinoic acid signaling. Proc Natl Acad Sci U S A 110, 16121–16126, doi:10.1073/pnas.1305937110 (2013). [PubMed: 24043786]
51. Kiefer FW et al. Retinaldehyde dehydrogenase 1 coordinates hepatic gluconeogenesis and lipid metabolism. Endocrinology 153, 3089–3099, doi:10.1210/en.2011-2104 (2012). [PubMed: 22555438]
52. Kiefer FW et al. Retinaldehyde dehydrogenase 1 regulates a thermogenic program in white adipose tissue. Nat Med 18, 918–925, doi:10.1038/nm.2757 (2012). [PubMed: 22561685]
53. Ginestier C et al. ALDH1 is a marker of normal and malignant human mammary stem cells and a predictor of poor clinical outcome. Cell Stem Cell 1, 555–567, doi:10.1016/j.stem.2007.08.014 (2007). [PubMed: 18371393]
54. van den Hoogen C et al. High aldehyde dehydrogenase activity identifies tumor-initiating and metastasis-initiating cells in human prostate cancer. Cancer Res 70, 5163–5173, doi:10.1158/0008-5472.CAN-09-3806 (2010). [PubMed: 20516116]
55. Corti S et al. Identification of a primitive brain-derived neural stem cell population based on aldehyde dehydrogenase activity. Stem Cells 24, 975–985, doi:10.1634/stemcells.2005-0217 (2006). [PubMed: 16293577]
56. Gao J et al. Integrative analysis of complex cancer genomics and clinical profiles using the cBioPortal. Sci Signal 6, pl1, doi:10.1126/scisignal.2004088 (2013).
57. Cerami E et al. The cBio cancer genomics portal: an open platform for exploring multidimensional cancer genomics data. Cancer Discov 2, 401–404, doi:10.1158/2159-8290.CD-12-0095 (2012). [PubMed: 22588877]
58. Pena-Llopis S et al. BAP1 loss defines a new class of renal cell carcinoma. Nat Genet 44, 751–759, doi:10.1038/ng.2323 (2012). [PubMed: 22683710]

59. Morgan CA, Parajuli B, Buchman CD, Dria K & Hurley TDN,N-diethylaminobenzaldehyde (DEAB) as a substrate and mechanism-based inhibitor for human ALDH isoenzymes. Chem Biol Interact 234, 18–28, doi:10.1016/j.cbi.2014.12.008 (2015). [PubMed: 25512087]
60. Kadoch C & Crabtree GR Reversible disruption of mSWI/SNF (BAF) complexes by the SS18-SSX oncogenic fusion in synovial sarcoma. Cell 153, 71–85, doi:10.1016/j.cell.2013.02.036 (2013). [PubMed: 23540691]
61. Schick S et al. Systematic characterization of BAF mutations provides insights into intracomplex synthetic lethalities in human cancers. Nat Genet 51, 1399–1410, doi:10.1038/s41588-019-0477-9 (2019). [PubMed: 31427792]
62. Helming KC et al. ARID1B is a specific vulnerability in ARID1A-mutant cancers. Nat Med 20, 251–254, doi:10.1038/nm.3480 (2014). [PubMed: 24562383]
63. Lessard J et al. An essential switch in subunit composition of a chromatin remodeling complex during neural development. Neuron 55, 201–215, doi:10.1016/j.neuron.2007.06.019 (2007). [PubMed: 17640523]
64. Wilson BG et al. Residual complexes containing SMARCA2 (BRM) underlie the oncogenic drive of SMARCA4 (BRG1) mutation. Mol Cell Biol 34, 1136–1144, doi:10.1128/MCB.01372-13 (2014). [PubMed: 24421395]
65. Yan Z et al. PBAF chromatin-remodeling complex requires a novel specificity subunit, BAF200, to regulate expression of selective interferon-responsive genes. Genes Dev 19, 1662–1667, doi:10.1101/gad.1323805 (2005). [PubMed: 15985610]
66. Kia SK, Gorski MM, Giannakopoulos S & Verrijzer CP SWI/SNF mediates polycomb eviction and epigenetic reprogramming of the INK4b-ARF-INK4a locus. Mol Cell Biol 28, 3457–3464, doi:10.1128/MCB.02019-07 (2008). [PubMed: 18332116]
67. Wilson BG et al. Epigenetic antagonism between polycomb and SWI/SNF complexes during oncogenic transformation. Cancer Cell 18, 316–328, doi:10.1016/j.ccr.2010.09.006 (2010). [PubMed: 20951942]
68. Kim KH et al. SWI/SNF-mutant cancers depend on catalytic and non-catalytic activity of EZH2. Nat Med 21, 1491–1496, doi:10.1038/nm.3968 (2015). [PubMed: 26552009]
69. Xue Y et al. The human SWI/SNF-B chromatin-remodeling complex is related to yeast rsc and localizes at kinetochores of mitotic chromosomes. Proc Natl Acad Sci U S A 97, 13015–13020, doi:10.1073/pnas.240208597 (2000). [PubMed: 11078522]
70. Cojoc M et al. Aldehyde Dehydrogenase Is Regulated by beta-Catenin/TCF and Promotes Radioresistance in Prostate Cancer Progenitor Cells. Cancer Res 75, 1482–1494, doi:10.1158/0008-5472.CAN-14-1924 (2015). [PubMed: 25670168]
71. Hoshino Y et al. Smad4 Decreases the Population of Pancreatic Cancer-Initiating Cells through Transcriptional Repression of ALDH1A1. Am J Pathol 185, 1457–1470, doi:10.1016/j.ajpath.2015.01.011 (2015). [PubMed: 25769430]
72. Zhao D et al. NOTCH-induced aldehyde dehydrogenase 1A1 deacetylation promotes breast cancer stem cells. J Clin Invest 124, 5453–5465, doi:10.1172/JCI76611 (2014). [PubMed: 25384215]
73. Devalaraja S et al. Tumor-Derived Retinoic Acid Regulates Intratumoral Monocyte Differentiation to Promote Immune Suppression. Cell 180, 1098–1114 e1016, doi:10.1016/j.cell.2020.02.042 (2020). [PubMed: 32169218]

Implications

This study implicates the SWI/SNF subunit and tumor suppressor PBRM1 in the regulation of promoter histone modifications and retinoic acid biosynthesis and signaling pathways in ccRCC and functionally validates one such target gene, the aldehyde dehydrogenase ALDH1A1.

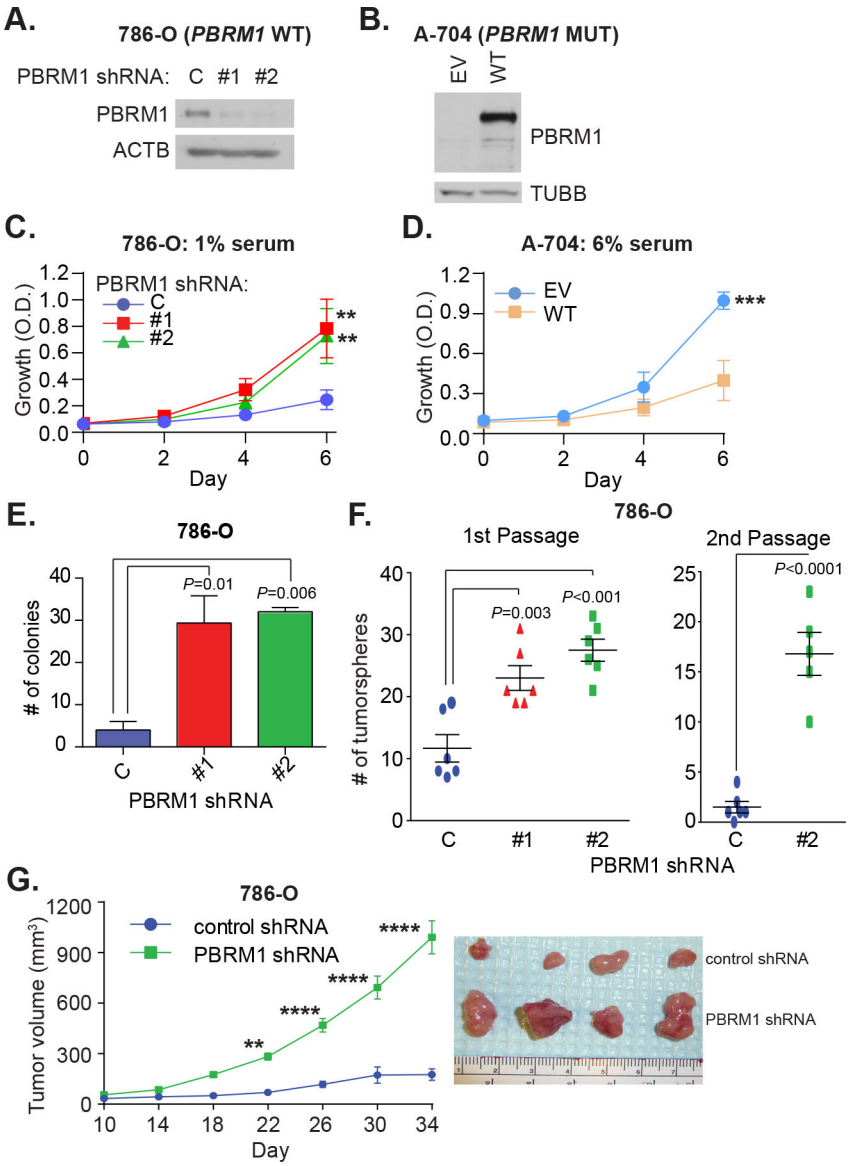

Fig. 1. PBRM1 deficiency in ccRCC cell lines increases tumorigenic potential.

Western blot analysis of PBRM1 protein levels in A) 786-O cells transduced with lentiviruses containing a non-targeting shRNA (labelled as “C”), or PBRM1-targeting shRNA (labelled as “#1” or “#2”), and B) A-704 cells transduced with empty-vector containing retrovirus (EV), or retrovirus containing wild-type PBRM1 with a C-terminal V5 tag (WT). 2D growth curves at the indicated serum concentration of C) 786-O cells (n=3/timepoint for each line, from independent experiments) and D) A-704 cells (n=3/timepoint for each line, from independent experiments). Two-way ANOVA using Tukey’s multiple comparisons test was performed on each set of growth curves. E) Colony formation in soft agar for the indicated 786-O cells. Error bars represent standard errors of the mean (SEM), n=3/line, from independent experiments; statistical testing comparing all column means was performed using ordinary one-way ANOVA with Tukey’s multiple comparisons test. F) Tumorsphere-forming capacity of 786-O lines: left panel - number of tumorspheres formed

initially (1st passage); right panel - number of tumorspheres formed for control and PBRM1 shRNA #2 lines after dissociating cells from 1st passage and replating (2nd passage). Bars represent SEM for n=5–6, from independent experiments; for left panel, statistical testing comparing all column means was performed using ordinary one-way ANOVA with Tukey's multiple comparisons test; for right panel, unpaired t-test was used. G) Tumor xenograft growth curves of 786-O control and PBRM1 shRNA #2 cells, 10^6 cells/injection, n=4/line. Two-way ANOVA with Tukey's multiple comparisons test was performed. Right panel – excised tumor xenografts after mice euthanasia on day 34 post-injection. * $P<0.05$; ** $P<0.01$; *** $P<0.001$.

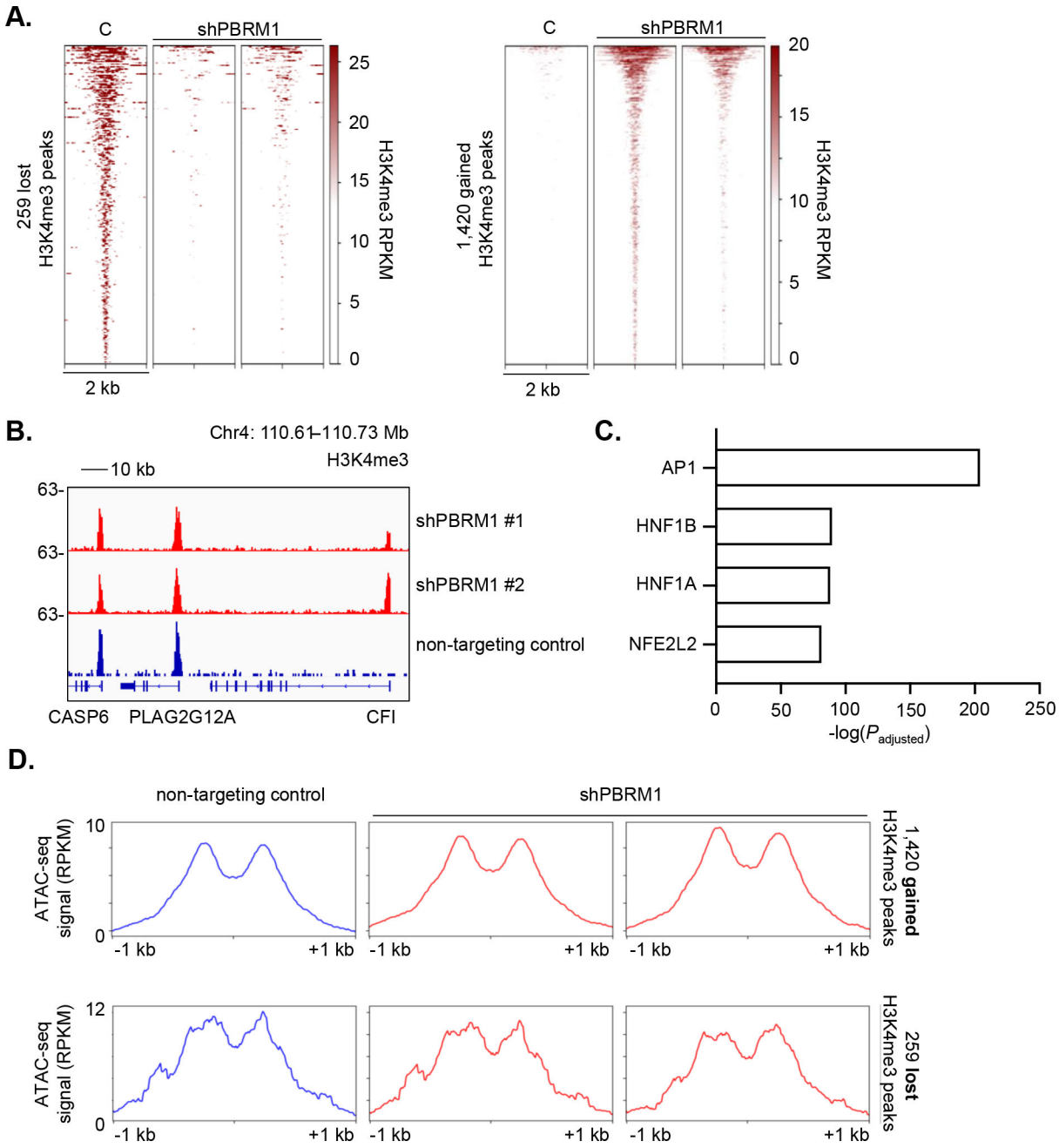

Fig. 2. Loss of PBRM1 results in significantly gained H3K4me3 peaks across the epigenome.

A) Heatmap of H3K4me3 signal (RPKM) at 259 lost (left) and 1,420 gained (right) H3K4me3 peaks with PBRM1 knockdown in 786-O cells. Two independent PBRM1 shRNA lines are shown compared to the non-targeting shRNA control ("C") line. B) H3K4me3 ChIP-seq track showing an example of a gained H3K4me3 peak in both PBRM1 shRNA lines (red) compared to the control line (blue). Two H3K4me3 peaks at other locations are included to show scale and specificity of the change. c) TRAP motif analysis of top transcription factor motifs enriched at open chromatin regions (as determined by ATAC-seq) at the 1,420 gained H3K4me3 loci. D) Metagene plot of ATAC-seq signal (RPKM) at the

1,420 gained (top) and 259 lost (bottom) H3K4me3 peaks in 786-O PBRM1 shRNA cells (red) and control cells (blue).

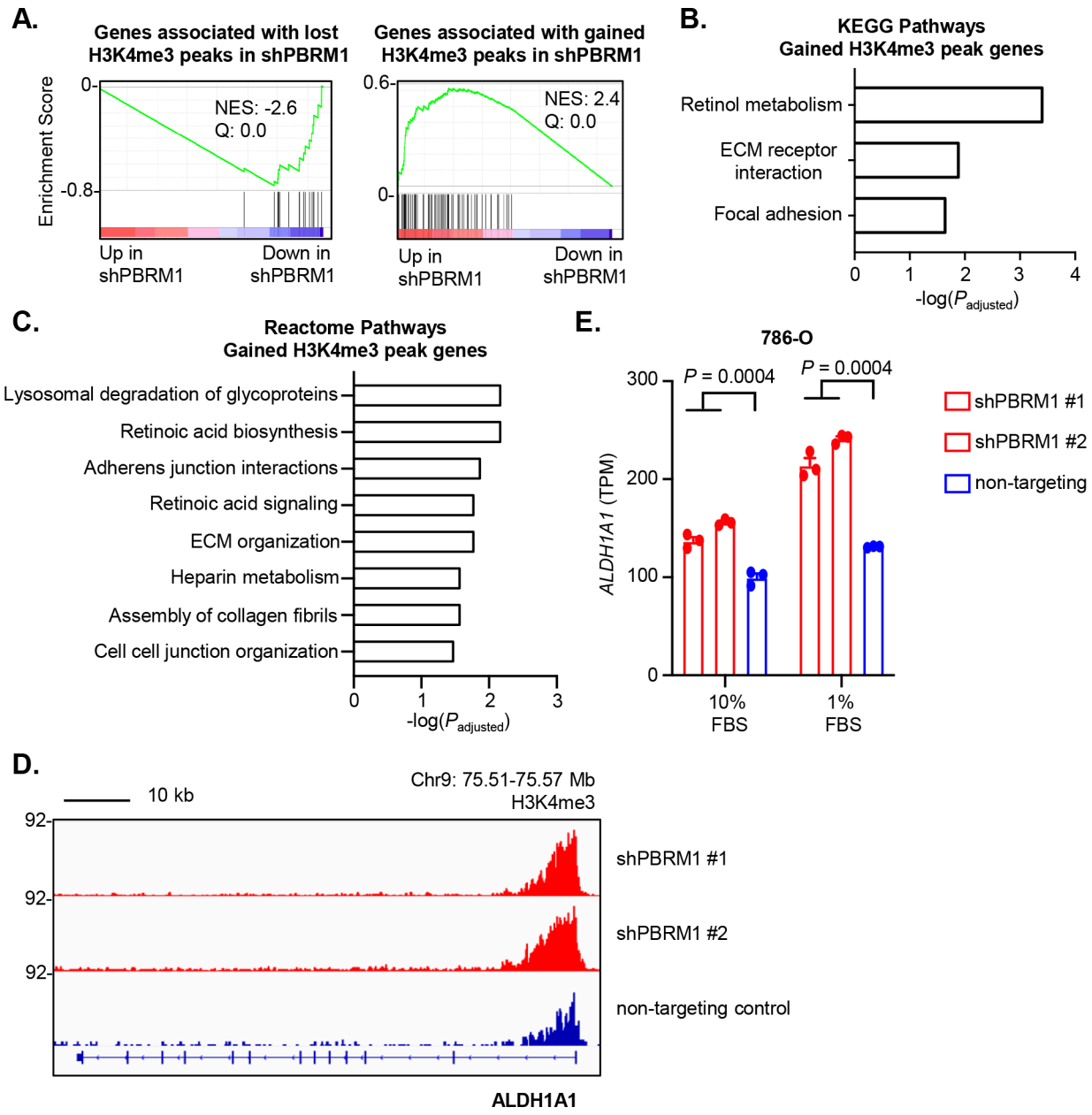

Fig. 3. Gained H3K4me3 peaks following PBRM1 loss are associated with a retinoic acid signature.

A) GSEA validation of derived gene signatures associated with 259 lost and 1,420 gained H3K4me3 peaks. B-C) Enrichr pathway analysis of the gained H3K4me3 peak gene signature, using the B) KEGG and C) Reactome pathway databases. D) H3K4me3 ChIP-seq tracks at the *ALDH1A1* locus in PBRM1 shRNA cells (red) and non-targeting control cells (blue). E) RNA-seq expression of *ALDH1A1* in PBRM1 shRNA cells (red) and non-targeting control cells (blue) at the indicated FBS concentration.

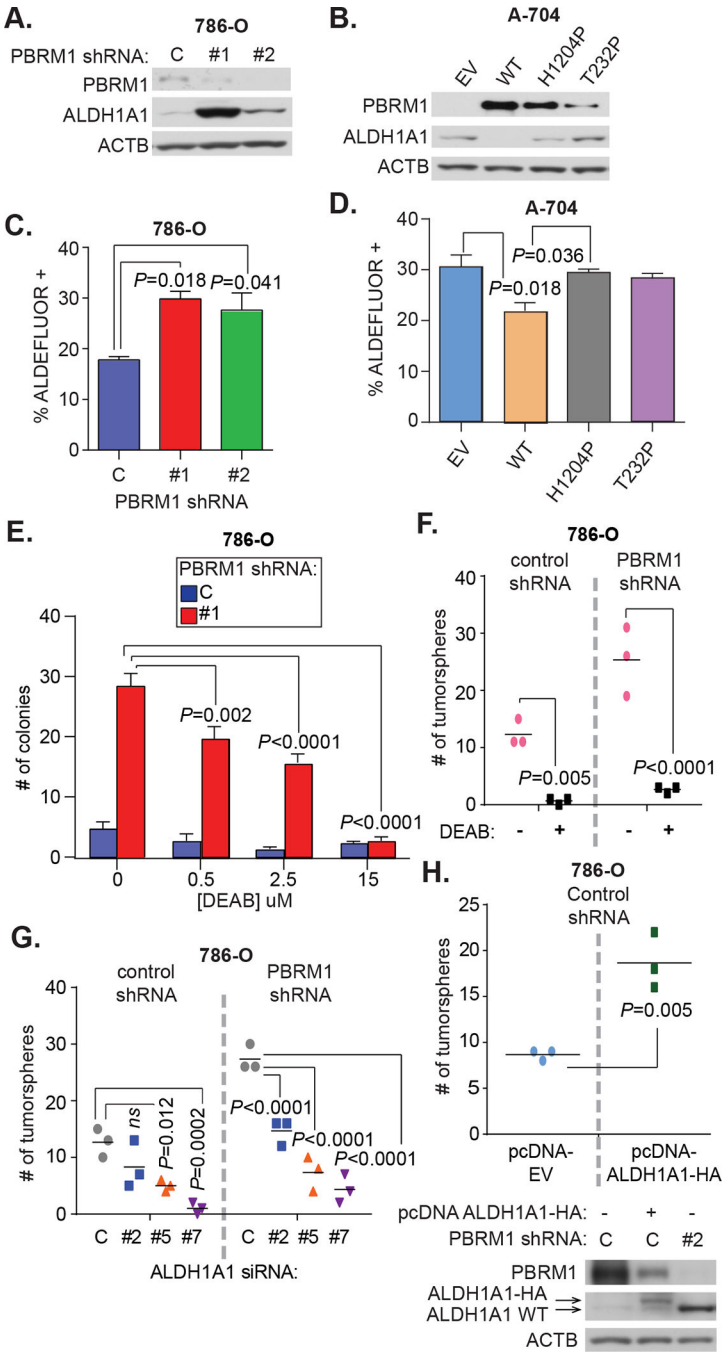

Fig 4. PBRM1 deficiency results in higher ALDH1A1 expression which increases tumorigenic potential.

Western blot analysis of ALDH1A1 protein levels in A) 786-O cells and B) A-704 cells. For C) 786-O and D) A-704 cells, the ALDEFLUOR assay was used to measure the percent of cells that were ALDEFLUOR-positive. n=3/line, error bars represent SEM, from independent experiments, and statistical testing comparing all column means was performed using ordinary one-way ANOVA with Tukey's multiple comparisons test. E) Colony formation in soft-agar of 786-O control and PBRM1 shRNA #1 cells. Increasing doses of DEAB were mixed in with soft-agar at the time of plating. n=3/line at each dose,

error bars represent SEM, from independent experiments, and statistical testing comparing the 0 μM treated condition vs. higher doses within a cell line was performed using an ordinary two-way ANOVA with Tukey's multiple comparisons test, with no significant differences among the control cells. F and G) Tumorsphere assays in 786-O control and PBRM1 shRNA #2 lines. In F), vehicle control or DEAB (15 μM) was added to tumorsphere media at the time of plating. In G), cells were transfected with non-targeting siRNA (C) or 1 of 3 *ALDH1A1*-targting siRNAs (#2, #5, or #7) 24 hr before plating for tumorsphere assay. H) 786-O control cells were transfected with empty-vector control plasmid (pcDNA-EV) or a plasmid expressing human influenza hemagglutinin (HA)-tagged ALDH1A1 (pcDNA-ALDH1A1-HA). Bottom panel - Western blot analysis comparing ALDH1A1 levels in 786-O control cells transfected with EV-control (left lane) or ALDH1A1-HA (middle lane), or non-transfected PBRM1 shRNA #2 cells (right lane). Top panel – tumorsphere formation in 786-O control cells transfected with the indicated plasmids. For parts F-H, n=3/condition, from independent experiments; for F-G, statistical testing was performed using an ordinary two-way ANOVA with the Sidak method to correct for multiple comparisons between conditions within cell lines; for part H, an unpaired t-test was performed.

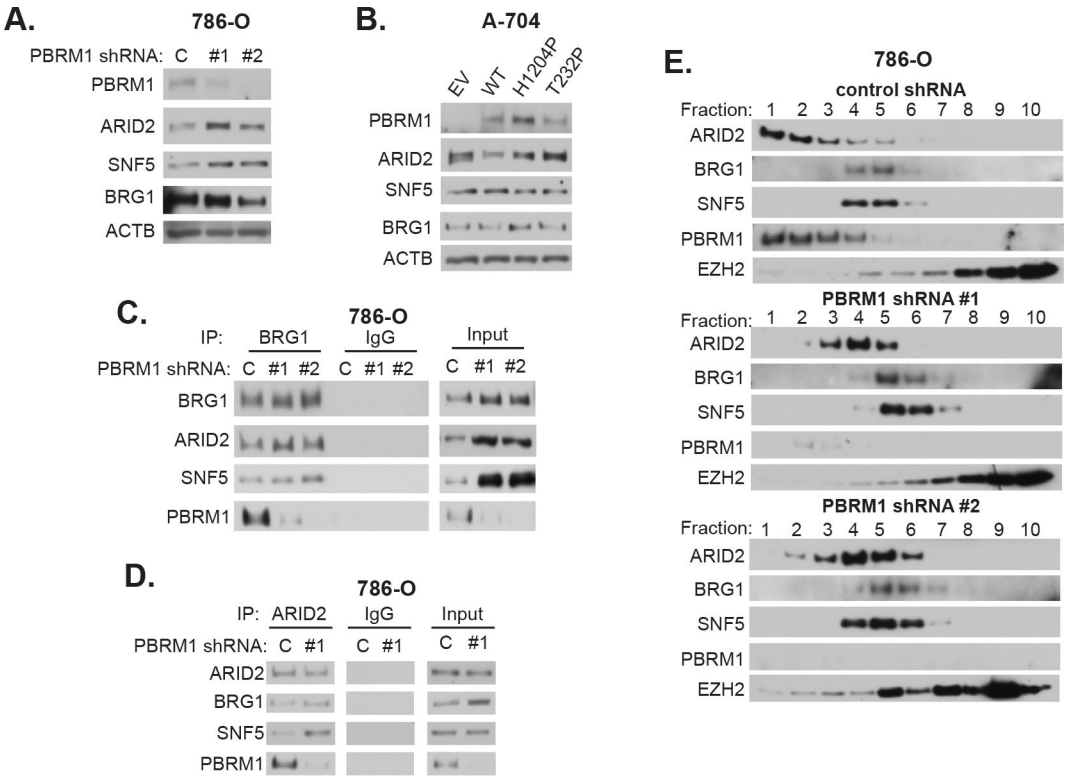

Fig 5. With PBRM1 deficiency, ARID2 is more highly expressed and remains bound to other SWI/SNF subunits.

Western blot analysis of the indicated PBAF complex subunits in A) 786-O cells and B) A-704 cells. Immunoprecipitation (IP) experiments in 786-O cells for C) BRG1 and D) ARID2. Matched isotype IgG was used for control IPs. Inputs are aliquots taken from pre-cleared nuclear extracts before the IPs were performed. E) Western blot analysis of heavy fractions (#1–10, out of 24 total) from glycerol gradient fractionation of nuclear extracts from 786-O cells. The PRC2 protein EZH2 is shown for comparison.

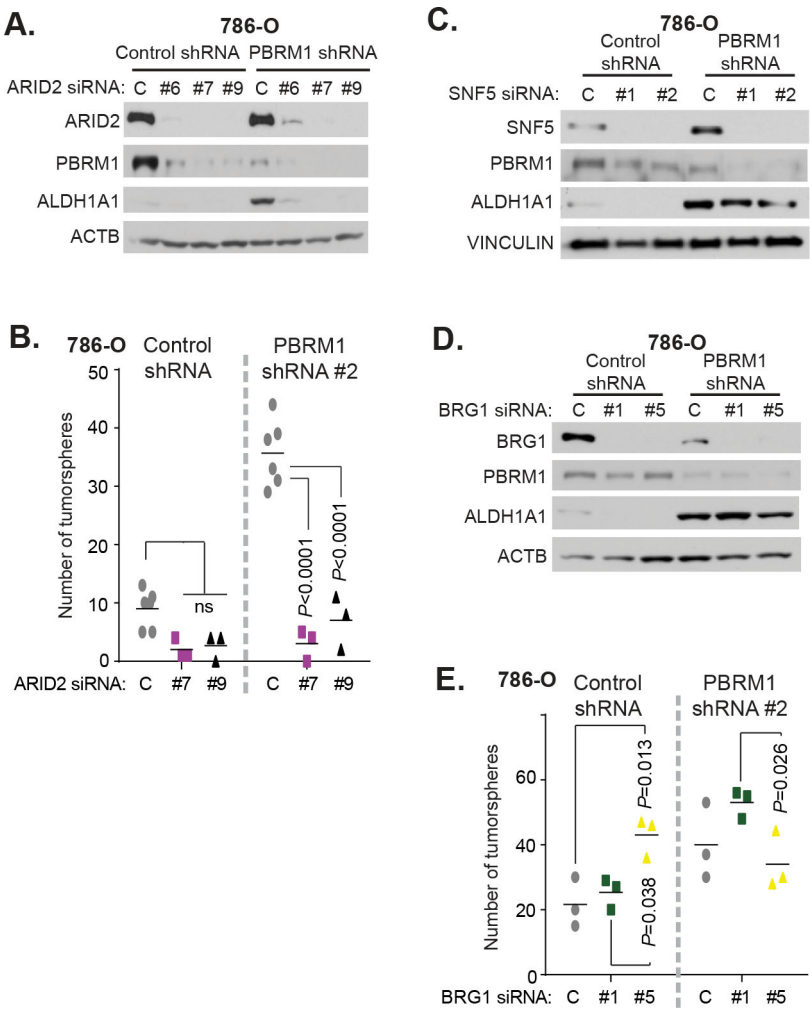

Fig 6. ARID2 is required for increased ALDH1A1 expression and tumorsphere formation, whereas BRG1 and SNF5 are dispensable.

A, C, D) Western blot analysis exploring effects of knocking down A) ARID2, C) SNF5, and D) BRG1 in 786-O control and PBRM1 shRNA #1 cells. A non-targeting siRNA was used as a control (labeled “C”). B and E) Tumorsphere assays in 786-O control and PBRM1 shRNA #2 cells. Cells were transfected with non-targeting siRNA (labeled “C”) or targeting siRNAs 24 hr before plating for the tumorsphere assay. n=3–6/condition, from independent experiments; statistical testing was performed using an ordinary two-way ANOVA with Tukey’s multiple comparisons test between conditions within cell lines.